Journal of Materials Chemistry C

ROYAL SOCIETY OF CHEMISTRY

PAPER

View Article Online
View Journal | View Issue

Cite this: J. Mater. Chem. C, 2023, 11, 4070

Untangling the role of the carbon matrix in the magnetic coupling of Ni@C nanoparticles with mixed FCC/HCP crystal structures

Mona Fadel, [a] F. Julián Martín-Jimeno,[b] M. P. Fernández-García, [a] Fabián Suárez-García,[b] Juan Ignacio Paredes, [b] J. H. Belo,[c] J. P. Araújo,[c] Alaa Adawy, [d] David Martínez-Blanco,[e] Pablo Álvarez-Alonso, [af] Jesús A. Blanco [a] and Pedro Gorria [*af]

Nowadays, Ni@C nanostructured materials are attracting a great deal of attention due to their multiple catalytic or magnetic functionalities. In this article we report on the investigation of the correlation between the microstructure and magnetic properties of Ni nanoparticles embedded in a carbon matrix. The samples were obtained following a two-step procedure that ensures protection against nanoparticle oxidation, and was carried out in the following way: (i) the synthesis of a nickel-imidazole-based metal–organic framework (MOF) by a simple method in an aqueous medium at moderate temperature (95 °C); and (ii) carbonization of the MOF at different temperatures between 400 and 600 °C to obtain a carbon-supported hybrid material, containing Ni nanoparticles with an "artichoke-like" morphology, where a Ni-FCC core is surrounded by "bracts" of Ni-HCP and Ni_3C. The average size of the nanoparticle slightly changes from 7 to 10 nm as the carbonization temperature is increased, but the Ni-FCC core diameter ranges from 3 to around 6 nm. We show how the information obtained on the evolution of the magnetic behaviour with carbonization temperature, using X-ray diffraction and electron microscopy, complements each other by providing consistent structural and magnetic characteristics of the investigated Ni@C nanoparticles. In fact, this joint analysis allows us to explain the formation and transformation of different Ni-based crystalline phases along the synthesis process, including Ni_3C and Ni with both hexagonal and cubic crystalline structures. The amount of conventional Ni-FCC is below 10 wt% for the sample treated at 400 °C and it can reach up to 50 wt% for that treated at 600 °C. Finally, based on our current findings we propose an explanation for understanding the magnetic properties of Ni@C, in which the Ni-FCC core spins mainly govern the magnetic coupling of the whole system.

Received 20th January 2023,
Accepted 23rd February 2023

DOI: 10.1039/d3tc00257h

rsc.li/materials-c

Introduction

Nickel nanoparticles are intensively investigated because their physical–chemical properties make them highly attractive for several key applications, such as anode soil fuel cells, conductivity electrolytic layers, automotive catalytic converters, propellent and sintering additives, biocompatible antibacterial agents, magnetic separation, magnetic fluid and catalysts, or electromagnetic absorbers for applications in telecommunication technologies.[1–7]

In the field of transition metal catalysis, nickel has several oxidation states and might be seen just as the younger and low-cost sibling of palladium or platinum as it lies just above them in the periodic table and thus, can readily perform many of the same elementary reactions as Pd and Pt. However, the catalytic activity of Ni is reduced, and its industrial applications are limited when it forms large aggregates. Therefore, it is interesting to follow strategies that allow the formation of small Ni clusters or nanoparticles (NPs),[8,9] and more importantly, obtain them in supported matrices that prevent their aggregation. Owing to their unique properties, carbon supports are specially interesting among other support options because they provide low density, small weight, high chemical and thermal stabilities, and tuneable porous texture. Therefore, heterogeneous carbon

[a] Departamento de Física, Universidad de Oviedo, E-33007 Oviedo, Spain. E-mail: pgorria@uniovi.es
[b] Instituto de Ciencia y Tecnología del Carbono, INCAR-CSIC, C/Francisco Pintado Fe 26, 33011 Oviedo, Spain
[c] IFIMUP, Departamento de Física e Astronomia da Faculdade de Ciências da Universidade do Porto, Rua do Campo Alegre, 687, 4169-007 Porto, Portugal
[d] Unidad de Microscopia Electrónica y Nanotecnología, SCTs, Universidad de Oviedo, 33006 Oviedo, Spain
[e] Unidad de Difracción de rayos X, SCTs, Universidad de Oviedo, 33006 Oviedo, Spain
[f] IUTA, EPI, Universidad de Oviedo, 33203 Gijón, Spain

catalysts were obtained through supporting Ni NPs on graphene, porous carbons, carbon nanotubes, *etc.*[3,10,11] Moreover, hybrid carbon supported materials with dispersed metallic or metal–oxide NPs forming metal–organic frameworks (MOFs) are currently being extensively investigated due to their promising capabilities towards highly efficient microwave absorbers and attenuators.[12–14]

In this regard, an original strategy towards carbon-supported Ni NPs is to obtain sacrificial materials based on MOFs with a large content of highly dispersed metallic NPs upon heat treatment (carbonization).[15] During the last decade some works have reported MOFs containing metallic ions or clusters, synthesized and pyrolyzed at high temperature to trigger thermal decomposition of MOFs, thus providing metal or metal–oxide/C nanohybrids.[16–18] However, there are only a few examples in the literature of Ni-containing MOFs that have been pyrolyzed to produce Ni@C catalysts after short reaction times (<30 min), moderate temperatures (95 °C) and following environmentally friendly routes. Recently, a two-step procedure towards carbon-supported Ni NPs that fulfils those requirements was developed and relies on a simple aqueous synthesis of a MOF and its subsequent carbonization strategy.[19] It should be noted that this Ni-based MOF was named NiOF by analogy with zeolitic imidazolate frameworks (ZIF) because Ni acts as the coordinating metal and imidazolate as the ligand. In the first step of the procedure, NiOF itself was synthesized, whereas in the second step Ni NPs embedded in carbon matrices were obtained by carbonization. During the carbonization process different Ni-based crystalline phases are found: Ni_3C, hexagonal close-packed (HCP) and face-centred cubic (FCC) crystal structures.[19]

As is well known a FCC crystalline structure is the stable phase of nickel (Ni-FCC, PDF 03-065-2865) at ambient pressure and at temperatures up to its melting point (1726 K). However, the addition of a small amount of light elements, such as N, C, B or H, can stabilize the HCP crystalline structure (Ni-HCP, JCPDS file no. 45-1027).[20] Theoretical predictions provide lattice parameter values for Ni-HCP of a = 2.500 Å and c = 3.980 Å,[21] similar to those reported for a Ni-HCP phase obtained during the thermal decomposition of Ni_3C NPs (a = 2.496 Å and c = 4.078 Å),[22] although some other works give values of a = 2.648–2.660 Å and c = 4.328–4.339 Å.[23,24] The latter values are close to those of Ni_3C in either rhombohedral (JCPDS file no. 77-0194) or HCP (JCPDS file no. 04-0853) crystal structures, $a \approx 2.6$ Å and $c \approx 4.3$ Å.[25] Moreover, it was reported that the close packed crystal structure of Ni_3C could be described by either a hexagonal unit cell or otherwise by a rhombohedral supercell with $a = \sqrt{3}\, a_{HEX}$ and $c = 3\, c_{HEX}$.[26,27] Consequently, it is extremely difficult to distinguish both phases, Ni-HCP and Ni_3C, by X-ray diffraction because the differences in the lattice spacing between Ni-HCP and rhombohedral Ni_3C crystalline structures are about 10^{-2} Å, and even smaller for Ni-HCP and Ni_3C-HCP (10^{-3} Å).[28]

To address this issue, some studies approached it from the magnetic point of view, reporting different Ni@C phases within the nanometer length-scale exhibiting diverse magnetic behaviour, which depends strongly on the synthesis procedure.[29–33] Although, Ni-HCP was theoretically predicted to exhibit ferromagnetic behaviour with a magnetic moment value close to that of Ni-FCC (0.59–0.76μ_B or 56.1–72.3 emu g^{-1}),[31,32] other experimental works claimed nonmagnetic,[33] antiferromagnetic,[24] or even weakly ferromagnetic[34,35] behaviour in Ni-HCP. Moreover, it was suggested that the weak magnetism of Ni-HCP may be triggered by Ni_3C, which was mistakenly identified as Ni-HCP.[28] However, the observation of a tiny magnetic signal in Ni_3C,[25,26,36] that is assumed as a non-magnetic phase,[26,37,38] could be ascribed to small Ni-FCC impurities.[27,37] In summary, a consistent and comprehensive explanation of the discrepancies between theory and experiments concerning the magnetic behaviour of the Ni@C hybrid nanocomposites is still lacking.

In the present paper, we have performed a detailed experimental investigation into Ni@C NPs obtained *via* an environmentally friendly synthesis method at temperatures between 400 and 600 °C. We intend to shed light on the evolution of the different Ni-containing phases that are formed depending on the synthesis conditions (Ni-FCC, Ni-HCP and Ni_3C) and at the same time, reveal the true magnetic character of Ni-HCP and Ni_3C. For this purpose, we have thoroughly analysed the crystalline structure, morphology and magnetic properties by means of different structural and physical characterization methodologies including X-ray diffraction (XRD), high resolution transmission electron microscopy (HRTEM) and magnetometry.

Experimental methods

Synthesis procedure

Nickel acetate tetrahydrate ($Ni(OAc)_2{\cdot}4H_2O$) purchased from Alfa Aesar and 2-methylimidazole (2-mIm) from Acros Organics were used as starting materials. The samples were obtained following the two-step procedure to obtain Ni@C catalysts, as previously reported in ref. 19. Basically, it consists of: (i) the synthesis of a nickel–imidazole MOF (NiOF) by a simple method in an aqueous medium and (ii) a thermal treatment at different carbonization temperatures to obtain a hybrid material formed by Ni NPs embedded in a carbon matrix.

Initially, 10 g of 2-mIm and 20 g of NiOAc were dissolved separately in 2 volumes of 50 ml of distilled water. The molar ratio between the reactants was [2-mIm]:[NiOAc] = 6:1. Secondly, both solutions were pre-heated separately at 95 °C, stirred, and purged under an Ar flow to avoid the surface oxidation of the formed material. Then, the NiOAc solution was poured into the 2-mIm solution, and the reaction occured immediately, leading to the formation of the nickel-imidazole complex, as evidenced by a colour change (from green to yellow-orange). After 30 min under vigorous stirring at 95 °C, the reaction was stopped by placing the solution in an ice bath. The formed powder was recovered after washing with distilled water by centrifugation until no coloration was observed in the supernatant. The obtained metal–organic framework (NiOF) was dried under vacuum for 6 h at 200 °C to remove the residues of the non-reacted 2-mIm molecules that occluded the pores of the material. Finally, the NiOF samples were heated in a horizontal tubular furnace with N_2 flux (99.999% purity)

at a heating rate of 5 °C min^{-1}. The heating temperatures were T = 400, 450, 500, 550 or 600 °C and accordingly, the samples will be labelled hereafter as S400, S450, S500, S550, and S600, respectively.

Material characterization

The Ni content of the samples was determined by thermogravimetric analysis (TGA) using an SDT Q600 device (TA Instruments). Room temperature X-ray powder diffraction (XRD) patterns were collected in the 2θ-range 35°–100° using a PANalytical X'Pert Pro diffractometer in a Bragg–Brentano geometry using Cu $K_{\alpha 1}$ radiation (1.5406 Å). A LaB_6 standard has been used for calibration purposes. The Rietveld refinement of the diffraction patterns has been performed using the FULLPROF package[39] and following the procedure developed in ref. 40 for nanostructured systems. Microstructural analysis was performed based on the parameters obtained during the Rietveld refinement. The fit was carried out using a Thompson–Cox–Hasting function describing the shape of the diffraction peaks, and to obtain information about the size and strain of the crystallites, we have used a generalized Scherrer-peak-broadening formula.[40]

TEM and HRTEM images were recorded using a JEOL 200-EXII and a JEOL-JEM-2100F microscope operating at 180 kV and 200 kV, respectively. The sample specimens were prepared by dispersing and sonicating a small amount of the powdered sample in ethanol. Afterwards, several drops of the resulting suspension were placed on Cu TEM grids with ultrathin carbon films, and finally the solvent was allowed to evaporate. After evaluating several TEM micrographs, the diameters of randomly selected particles (at least 300 from each sample) were estimated using ImageJ software,[41] to build the particle-size histograms and fit them using a log-normal distribution. Besides, interplanar distances were obtained from the HRTEM images or their fast-Fourier-transform (FFT).[42,43]

The temperature and magnetic field dependences of magnetization, $M(T)$ and $M(H)$ curves, were measured in a Quantum Design PPMS-14T platform equipped with a vibrating sample magnetometer (VSM) option at the University of Oviedo, and a MPMS 3 SQUID magnetometer placed at the Instituto de Física dos Materiais da Universidade do Porto (IFIMUP). The magnetization *vs.* temperature measurements were performed following conventional zero-field-cooling (ZFC) and field cooling (FC) procedures, to obtain the corresponding $M_{ZFC}(T)$ and $M_{FC}(T)$ curves, respectively. Firstly, the samples were cooled down from 300 K to 10 K in zero field, then a magnetic field (100 Oe) was applied and kept constant during the measurement of the $M_{ZFC}(T)$ curve on heating from 10 to 300 K. Subsequently, the $M_{FC}(T)$ curve was measured under the same value of the applied magnetic field on cooling down from 300 K to 10 K. In addition, the isothermal magnetization as a function of applied magnetic field, $M(H)$ curves, were collected at 5 K and 300 K in the ±55 kOe applied magnetic field range.

Results and discussion

TGA measurements

In Table 1 we show the results of the thermogravimetric analysis carried out under an air flow with the aim of determining the Ni content. The percentage of Ni increases progressively with the carbonization temperature from 38.3 wt% (S400 sample) to ≈49–50 wt% (S550 and S600 samples). This increase is due to the progressive loss of volatile matter from the carbonaceous fraction taking place during the carbonization process, where the degree of polycondensation and aromatization of the carbon framework increases with temperature.

Table 1 Nickel percentage derived from TGA measurements and values for the structural parameters obtained from TEM and XRD data. Note that the numbers in parentheses are the estimated error, except for the NP size that corresponds to the standard deviation (TEM)

Sample	TGA (wt% Ni)	$D_{TEM}(\sigma)$ (nm)	Ni_3C (wt%)	Ni-FCC (wt%)	Ni-FCC a (Å)	Ni-HCP (wt%)	Ni-HCP a (Å)/c (Å)
S400	38	7 (6)	46 (5)	10 (2)	3.530	44 (5)	2.53/3.59
S450	45	8 (3)		64 (4)	3.523	36 (3)	2.49/4.10
S500	48	7 (2)		67 (4)	3.523	33 (3)	2.49/4.10
S550	50	8 (2)		78 (5)	3.524	22 (3)	2.49/4.11
S600	49	10 (6)		75 (5)	3.524	25 (3)	2.49/4.11

Crystalline structure

Fig. 1 shows the room temperature XRD patterns of the samples together with the fits. All of them exhibit Bragg reflections associated with the FCC ($Fm\bar{3}m$) and HCP ($P6_3/mmc$) crystal structures of Ni, and the relative change of the intensities are related to the percentage of these phases that evolve with the carbonization temperature.

As is well known, the difference between the FCC and HCP crystal structures lies in the way that successive hexagonal layers are stacked upon one another in both structures. Therefore, as was anticipated above, there is an important overlapping of Bragg diffraction peaks associated with these crystal structures. In fact, the peaks observed at around 44°, 76° and 93° in 2θ are related to (111)/(002), (220)/(110) and (311)/(112) for Ni-FCC/Ni-HCP, respectively (see the top panel in Fig. 1).

Only using the Rietveld refinement method, we can separate both contributions refining the theoretical line profile due to both contributions until it matches the measured diffraction profile. Consequently, from the Rietveld analysis of the XRD patterns the percentage for the Ni-HCP phase decreases from 44 wt% (S400) to 25 wt% (S600), while the percentage of Ni-FCC grows from *ca.* 10 to 75 wt% for the same samples (see Table 1). Note that these phase-content values are related to the crystalline phases discriminated by XRD.

If we focus our attention on the XRD pattern of sample S400, apart from those belonging to Ni-FCC and Ni-HCP other reflections that can be ascribed to a nickel-carbide phase, Ni_3C, with either rhombohedral ($R\bar{3}c$) and hexagonal ($P6_3/mmc$) crystal structures have been identified. The value for the cell parameters of this Ni_3C phase (a = 4.515 Å, c = 12.876 Å and a = 2.686 Å, c = 4.306 Å; for the rhombohedral and hexagonal phases, respectively) are in good agreement with those previously reported during the thermal decomposition of Ni_3C NPs,[20] mechanically alloyed Ni_3C[26] and by theoretical calculations.[21,26] The broad and low-intensity diffraction peaks indicate the formation of small sized entities.

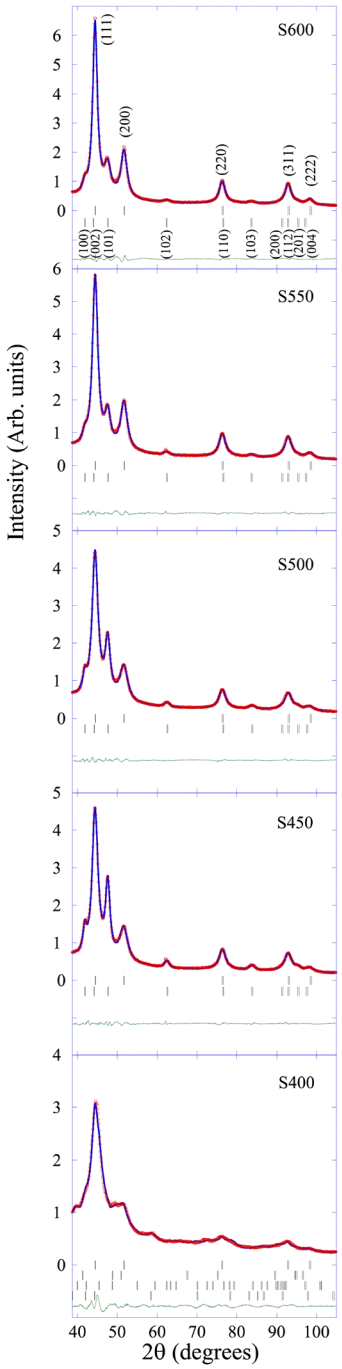

Fig. 1 Observed (red points) and calculated (blue lines) powder XRD patterns of the samples collected at room temperature. For samples S450 to S600 the first series of vertical bars correspond to the positions of the Bragg reflections associated with the crystal structure of Ni-FCC, and the second one with that of Ni-HCP. For sample S400 the vertical bars correspond to the positions of the Bragg reflections associated with the crystal structure of (from top to bottom) Ni-FCC, Ni-HCP, rhombohedral Ni_3C, and hexagonal Ni_3C. The observed-calculated difference pattern is depicted at the bottom of each figure.

In this regard, it is not possible to detect reflections corresponding to this Ni_3C crystalline structure in the samples synthesized at temperatures above 400 °C, although regions containing a small number of coherent lattice planes with lattice spacing corresponding to that of the Ni_3C crystalline structure can be observed in HRTEM images (even for the S600 sample, see below). The lack of X-ray diffraction peaks associated with the Ni_3C phase together with the existence of a considerable background signal in the XRD patterns supports the idea that higher carbonization temperatures favour a high degree of disorder, and consequently the degradation of the long-range order in this Ni-rich phase. Similar behaviour was reported during the relaxation and crystallization under controlled annealing of $Ni_{80}B_{20}$ metallic glass:[44] very small Ni_3B crystallites nucleate in Ni-rich regions with a high density of defects at the grain boundaries and surrounded by the amorphous Ni phase not permitting the establishment of long-range crystalline order.[45]

On the other hand, considering the broadening of the diffraction peaks and using the procedure based on a generalized Scherrer-peak-broadening formula,[38] it was possible to extract the corresponding sizes of the coherent diffraction crystallites. It is important to note the small diameter for the Ni NPs with a FCC crystal structure (between 3.8 and 5.6 nm) compared to other Ni NP systems.[46] This feature could be attributed to the presence of both Ni_3C and Ni-HCP phases covering the Ni-FCC cores that hinder growing up and sintering of the NP cores.[19] This circumstance will be of paramount relevance when explaining the magnetic properties of these Ni-based NPs (see below).

Microstructure and morphology

Considering that the relative Ni content of the samples depends on the carbonization temperature at which the synthesis of the samples takes place (see Table 1), we may expect a change in the number and size of Ni-NPs. In Fig. 2 several TEM and HRTEM images are displayed, where Ni-NPs with a quasi-spherical shape are randomly dispersed (dark spots in TEM images) within the carbon matrix. The histograms of the NP size distributions were obtained after measuring the diameters of at least 300 isolated NPs from several TEM images, and then, fitting those histograms to a log-normal distribution function characterized by its mean diameter (D_{TEM}) and standard deviation (σ) (see Fig. 3). These fits reveal a single broad distribution (ranging between 2–20 nm) for all samples with $D_{TEM}(\sigma)$ values of 7(6) nm, 8(3) nm, 7(2) nm, 8(2) nm and 10(6) nm for S400, S450, S500, S550, and S600, respectively (see Table 1).

Aiming to disentangle the complex mixture of crystalline phases identified from the XRD analysis and the carbonization temperature dependence of the evolution of those phases, we performed a careful HRTEM analysis for individual NPs in samples S400, S450, S500, S550 and S600 that confirmed their crystallinity with observable lattice fringes in several crystallographic directions. Since there are crystallographic planes in Ni-FCC, Ni-HCP, hexagonal Ni_3C and rhombohedral Ni_3C crystals (namely (111), (011), (002) and ($\bar{1}$23), respectively, with d_{hkl} spacing value of $\approx$ 2 Å), we can only, undoubtedly, distinguish these 4 crystalline structures using HRTEM analysis based on the presence of other relative d_{hkl}-spacing corresponding to other

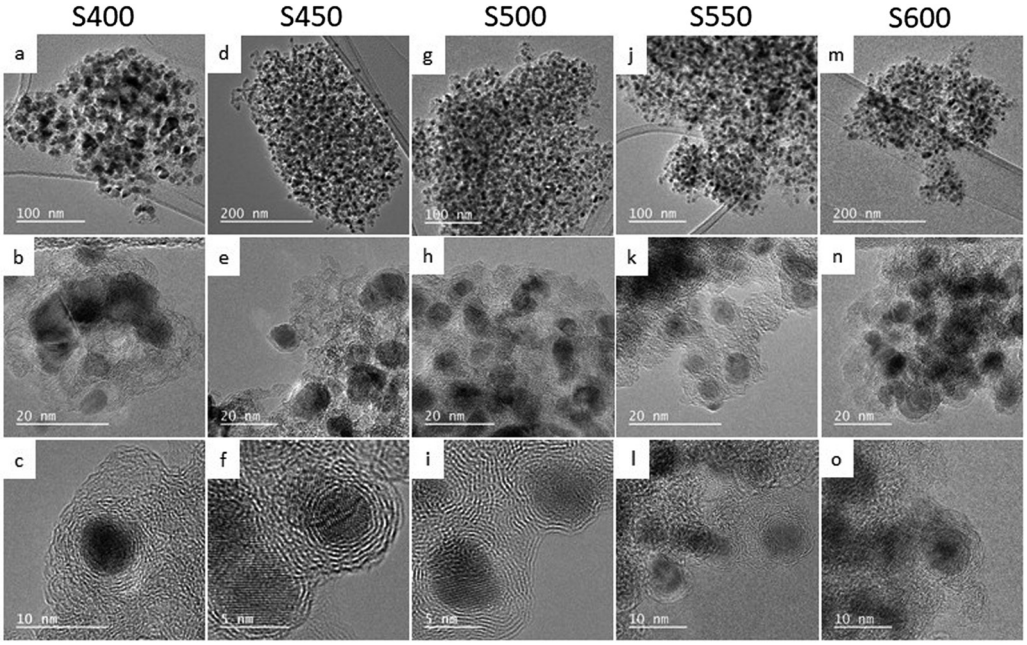

Fig. 2 Representative TEM and HRTEM images of samples (a–c) S400, (d–f) S450, (g–i) S500, (j–l) S550, and (m–o) S600.

related planes that can be attributed to only one crystallographic structure of those four. In Fig. 4a, a HRTEM image of a NP in the S400 sample is displayed in which only unidirectional lattice fringes could be clearly analysed, even after determining its autocorrelation function (see Fig. 4b).

Based only on HRTEM analysis, the observation of crystalline NPs with d_{hkl}-spacing values of $\approx$ 2 Å, with the absence of other analysable lattice fringes in other directions provide a statistical probability of 25% that these crystals could be attributed to Ni-FCC. However, relying on the statistical significance of Rietveld refinement of the XRD patterns, this sample should have around 10% of NPs belonging to Ni-FCC.

If this is the case, the existing Ni-FCC NPs could be difficult to be certainly identified, especially if they comprise the core of the NPs, since the microscopic resolution would be lacking under this defocusing imaging setting. Yet, with some defocusing, we could surely identify Ni-FCC crystallographic zones (Fig. 4c and d). Other crystallographic structures easily distinguished in this sample were Ni-HCP (Fig. 4e and f). For the S450 sample the HRTEM analysis confirmed the continued existence of Ni-HCP and Ni-FCC (Fig. 5).

It is worth mentioning here that the identified Ni-HCP crystallographic zones exhibit high image sharpness when compared to those of Ni-FCC. Further carbonization at 500 °C resulted in the growth of Ni NPs that undoubtedly accounts for the formation of cubic nickel nanocrystals (Ni-FCC) as was easily confirmed using the HRTEM images of the Ni NPs exhibiting multidirectional lattice fringes (Fig. 6a and b). Furthermore, in the sample treated at a carbonization temperature of 550 °C, HRTEM images revealed both relatively less-sharp images with crystallographic zones attributed to Ni-FCC, beside the sharp images with crystallographic zones that undoubtedly accounted for Ni-HCP (Fig. 6c–f).

The latter could be attributed to the difference between the different (de-)focusing degrees required to detect both polymorphs within a single nanocrystal, with Ni-FCC, most probably, occupying the nanocrystal cores (low-resolution crystallographic zones), while Ni-HCP occupying their outer shells (high-resolution crystallographic zones).

This explanation was confirmed clearly for the Ni-NPs synthesized at the highest carbonization temperature used in the current study, 600 °C, as shown in Fig. 7. Besides, rhombohedral Ni_3C could be still detected in the S600 sample (not shown). Therefore, it seems that, as a model picture, the NPs consist of a Ni-FCC core that changes to Ni-HCP in the outer region of the NP probably due to a hexagonal-type environment where a predominant Ni_3C phase is present (''artichoke-like'' morphology consisting of successive Ni-HCP and Ni_3C-like ''bracts'' anchored to the Ni-FCC core).

Additionally, it should be mentioned that the HRTEM images of the samples show the turbostratic carbon layers around Ni-NPs, most likely due to the progressive transformation of the NiOF into a Ni metal-carbon composite (see Fig. 2, bottom panel). This feature prevents the Ni-NPs from growing above 5–6 nm in diameter and protects these metallic Ni NPs from oxidation, as was confirmed by the absence of nickel oxide from either XRD and TEM/HRTEM analysis. Hence, we presume that the present synthesis procedure effectively facilitated the formation of relatively crystalline layers of turbostratic carbon covering most of the Ni-NPs (analogous to those recently found in Fe NPs[47]). This can be observed in Fig. 8 for sample S600, where an average distance of 0.35–0.36 nm between the stacked layers was measured. These findings suggest that the chemical synthesis route of the present work gives rise to a similar protection mechanism against NP oxidation to that already achieved following a pyrolysis-based synthesis strategy using sucrose for carbon-coated Ni NPs.[46]

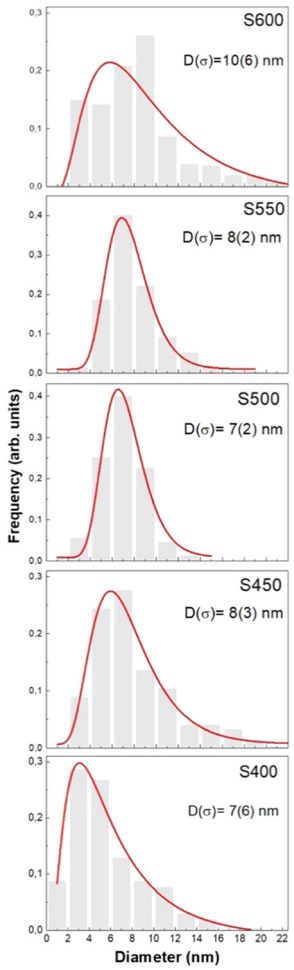

Fig. 3 Histograms of the total particle size distributions of the samples together with log-normal fits, providing mean diameters (D) and standard deviations (σ).

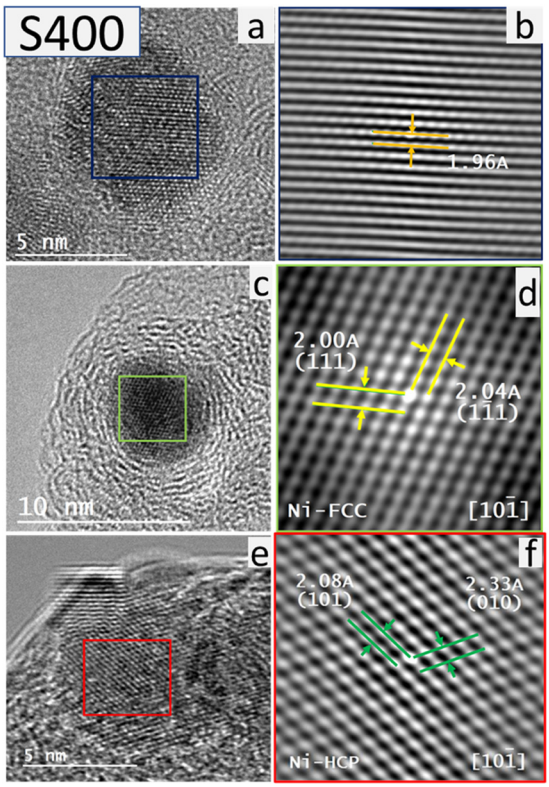

Fig. 4 HRTEM images for three representative NPs in sample S400 (left column) and their analysed autocorrelation micrographs for the areas indicated by coloured squares (right column). Analysing the NP displayed in (a) revealed lattice fringes in one direction (b) with d_{hkl}-spacing common between Ni-FCC, Ni-HCP, NiC-FCC and trigonal Ni_3C. (c) At specific defocusing for the NP, where it exhibits less image sharpness, crystallographic planes in the zonal axis [10$\bar{1}$] for Ni-FCC could be identified (d). Other two crystallographic zones accounting for Ni-HCP could be detected for the NPs displayed in (e and f), zone axis [10$\bar{1}$] of Ni-HCP.

Magnetic behaviour

The magnetization *versus* the applied magnetic field, $M(H)$, curves measured at $T = 300$ and 5 K under ZFC conditions are depicted in Fig. 9, and the values for the most relevant magnetic magnitudes obtained from the analysis can be found in Table 2. The $M(H)$ curves at 5 K are in fact hysteresis loops because they exhibit a non-zero coercive field (H_C) and remanent magnetization (M_r) related to the blocking of the spins in the NPs (see inset in Fig. 9b). The same $M(H)$ curves have also been measured under FC conditions; however, no difference is observed compared with ZFC-$M(H)$ curves, hence, there is no existence of any exchange-bias effect as observed in other Ni-based nanoparticulate systems,[48] and we can assume that only Ni-FCC contributes to the ferromagnetic signal (see below).

At $T = 300$ K the saturation regime for the magnetization (M_S) has not yet reached under an applied magnetic field of 50 kOe (see Fig. 9a), and the value of M_S estimated from the fit of the high applied field region ($H > 30$ kOe) of the $M(H)$ curves to a law of approach-to-saturation[49] increases with the carbonization temperature (see Table 2). It is worth noting that the sample with the smallest value for the M_S (S400) is that with the lowest percentage of Ni-FCC estimated from XRD patterns (see Table 1), slightly below 10%. If we assume that the Ni-FCC NPs possess the value of M_S for pure Ni (58.6 and 55.1 emu g^{-1} at $T = 5$ K and 300 K, respectively) and that this is the only phase contributing to M_S we reach an estimated value for the percentage of Ni-FCC around 9%, which is in excellent agreement with the value of 10% obtained from the analysis of the XRD pattern. The $M(H)$ curves for the other four samples display a much higher value (4 or even 5 times larger than that of sample S400) for the saturation magnetization, thus suggesting a larger amount of Ni-FCC in S450, S500, S550 and S600, as previously obtained by XRD.

Although some authors claim that Ni-HCP exhibits ferromagnetic behaviour[31,32] with a magnetic moment similar to that of Ni-FCC, around 0.6μ_B/Ni atom, the current magnetization data do not support such a claim. In the case that both HCP and FCC Ni phases were ferromagnetic a much larger signal under an applied field of 50 kOe, will be expected for sample S400, which is contrary to our findings. Moreover, our investigation suggests that the presence of carbon atoms in a solid solution in Ni can not only stabilize the HCP crystalline structure for Ni, as was previously mentioned above, but

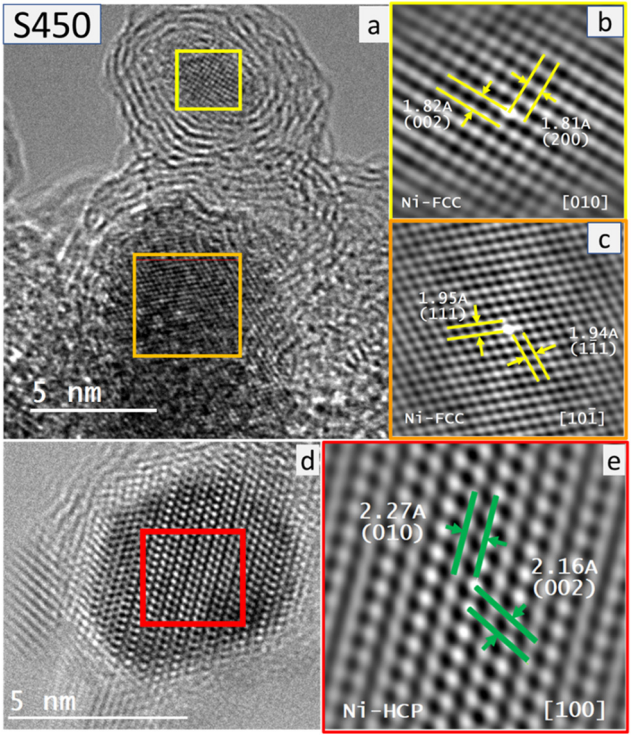

Fig. 5 Representative HRTEM images for three NPs in sample S450 (left) and their analysed autocorrelation micrographs for the areas indicated by coloured squares (right). (a) Two NPs exhibiting relatively low image sharpness (defocused) and the analysis of their autocorrelation micrographs revealed crystallographic planes belonging to two zone axes: (b) [010] and (c) [10$\bar{1}$] accounting for the Ni-FCC crystalline structure. (d) A nanoparticle displayed with high image sharpness (focused) revealed the crystallographic planes belonging to the zone axis [100] of the Ni-HCP crystalline structure (e).

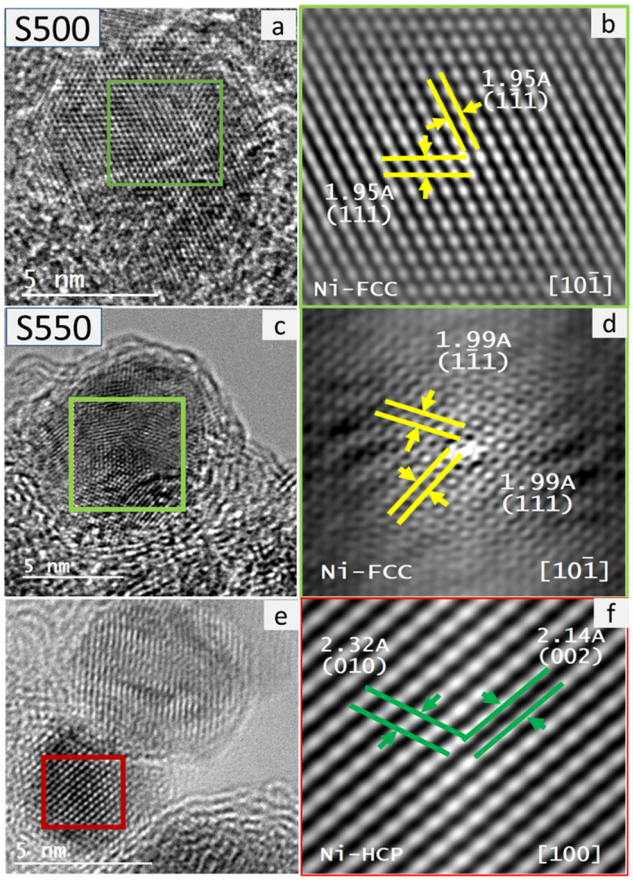

Fig. 6 Representative HRTEM images for three NPs in samples S500 and S550 (left column) and their analysed autocorrelation micrographs for the areas indicated by coloured squares (right column). (a) For S500, a nanoparticle displayed with high image sharpness (focused) and, (b) the analysis of its autocorrelation micrographs revealed crystallographic planes lying in the zone axis [10$\bar{1}$] that account for the Ni-FCC crystalline structure. (c) For S550, a nanoparticle displayed with relatively low image sharpness was hardly analysed to reveal the crystallographic planes also in the zone axis [10$\bar{1}$] of Ni-FCC shown in (d). A NP imaged with high image sharpness (focused) revealed the crystallographic planes belonging to the zone axis [100] of the Ni-HCP crystalline structure shown in (e and f).

concurrently, the coupling between the 3d–2p orbitals from the Ni–C bonding could establish a certain degree of covalence between these atoms, resulting in an antiferromagnetic or even non-magnetic character for the ground state of Ni_3C.[26]

These ideas are strongly supported by the observation of a drastic increase in the slope of the low temperature $M(H)$ curves measured at 5 K, far from being saturated (see Fig. 9b). The latter clearly indicates a strong paramagnetic contribution coming from the other two phases detected from both XRD and HRTEM experiments, namely, Ni_3C and Ni-HCP.

Therefore, magnetization *vs.* applied magnetic field measurements reinforces the previously discussed argument about the influence of the carbonization temperature on the mixture and transformation of the different Ni-based crystalline phases that appear in these materials. Furthermore, the values obtained for the saturation magnetization of the samples synthesized at temperatures above 400 °C are considerably smaller than expected, considering the relative percentages between the Ni-FCC and Ni-HCP phases obtained from XRD analysis (see Table 1). The latter suggests that a significant number of non-magnetic "dark-Ni" atoms is retained in a Ni-rich Ni_3C-like phase not detected by XRD due to the absence of long-range crystalline order but observed in HRTEM images as commented in the previous section. As a consequence of our experimental findings, we can ascertain that the only ferromagnetic phase at room temperature is Ni-FCC, while Ni_3C and Ni-HCP are paramagnetic.

In Fig. 10 the evolution of the Ni-containing phases is depicted as a function of carbonization temperature. It must be noted that the values corresponding to the Ni_3C phase in samples S450 to S600 have been estimated from magnetic measurements and the relative percentage between Ni-FCC and Ni-HCP extracted from the analysis of XRD patterns, because only in the case of the S400 sample the percentage of this phase can be estimated by XRD as discussed above.

The temperature dependence of the magnetization, $M(T)$ curves, measured following the ZFC and FC procedures between T = 5 K and T = 300 K under a magnetic field of 100 Oe is presented in Fig. 11.

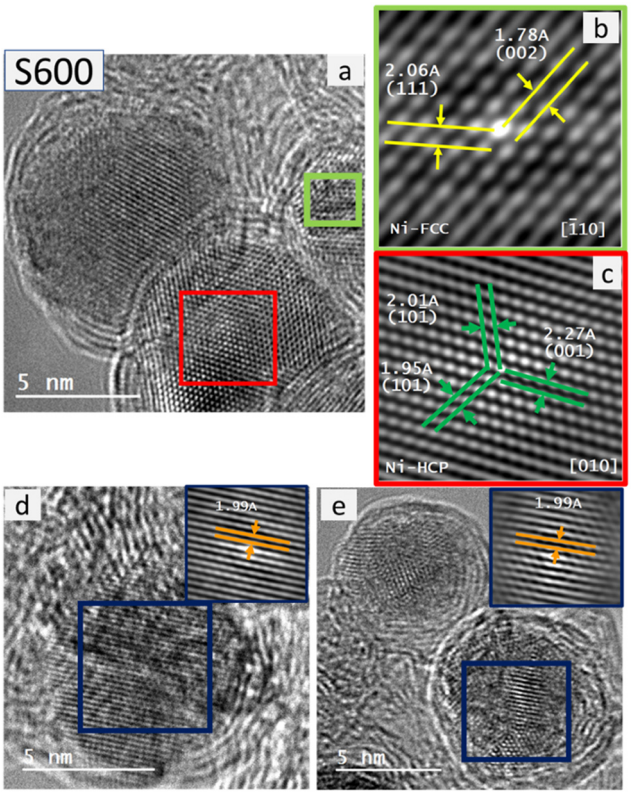

Fig. 7 Representative HRTEM images of four NPs in sample S600 and their analysed autocorrelation micrographs for the areas indicated by the coloured squares. (a) Three overlapping NPs could be observed in this image, with the one indicated with the green square lying at a relatively higher focal plane (defocused) when compared to the other NP, indicated with a red square, that lies in focus and thus shows high image sharpness. (b) The crystallographic analysis of the defocused NP revealed the crystallographic planes lying in the zone axis [1̄10] of the Ni-FCC crystalline structure, whereas; (c) the crystallographic analysis of the focused NP revealed crystallographic planes lying in the zone axis [010] of the of Ni-HCP crystalline structure. (d and e) Other defocused (soft) HRTEM images of two NPs revealed unidirectional lattice fringes with d_{hkl}-spacing $\approx$ 2Å that most probably accounts for d_{111} of the Ni-FCC core of the resultant NPs.

Even though the samples have different NP size distributions (see Fig. 3), all of them present qualitative features typical of single domain ferromagnetic NPs that remain blocked below a certain temperature (T_B, blocking temperature) and behave as superparamagnetic (SPM) for $T > T_B$. The temperature for the maximum of the $M_{ZFC}(T)$ curve is commonly ascribed to the average T_B of the system. Nevertheless, an increase of the NP average size gives rise to a shift of T_B towards higher temperatures and a wider temperature range for non-overlapping of $M_{ZFC}(T)$ and $M_{FC}(T)$ curves (irreversibility) that takes place at $T = T_{irr}$. Moreover, a broadening of the NP size distribution makes the maximum of the $M_{ZFC}(T)$ curve less defined, since the NPs enter the SPM regime at a wider interval of temperatures depending on their size distribution profile.

The $M(T)$ curves evidence a progressive evolution of the NP magnetic behaviour with the carbonization temperature. Sample S400 exhibits a canonical $M_{ZFC}(T)/M_{FC}(T)$ variation with

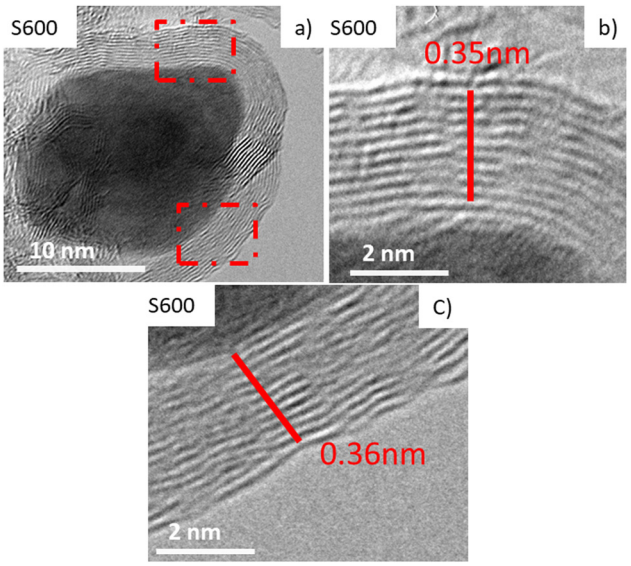

Fig. 8 Illustrative HRTEM images of sample S600. The red dotted rectangles on the image in (a) represent regions where graphene-like concentric layers are clearly identified surrounding a Ni-FCC NP. The red lines in (b and c) show the stacking of the turbostratic carbon layers. (See the text for more details).

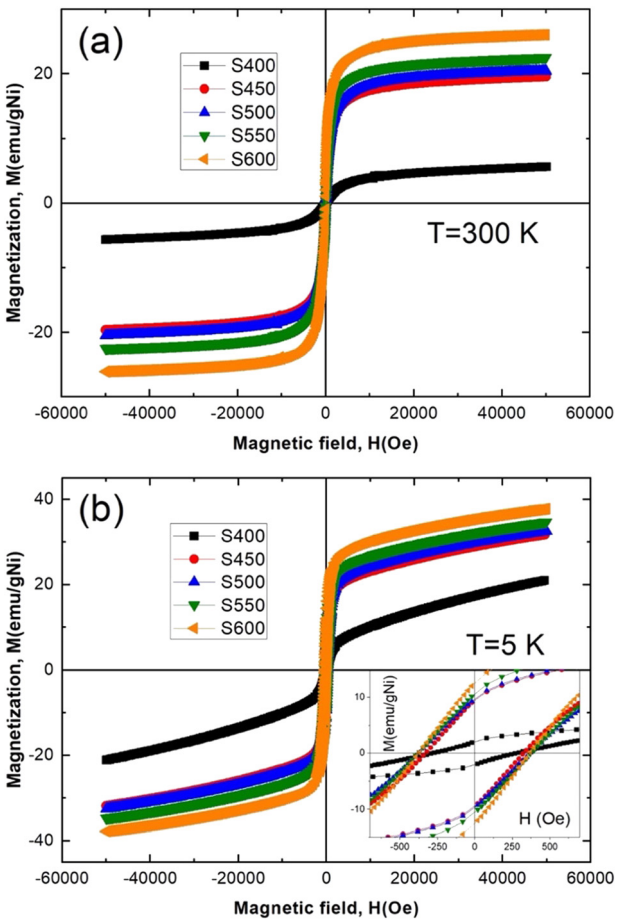

Fig. 9 Magnetization *vs.* applied magnetic field curves measured at T = 300 K (a) and T = 5 K (b). Note that insets show enlarged views of the origin region.

Table 2 Values of the estimated blocking temperature and saturation magnetization. Note that the number in parentheses is the estimated error

Sample	T_B (K)	M_S (T = 300 K) (emu g^{-1})	M_S (T = 5 K) (emu g^{-1})
S400	15 (1)	4.7 (5)	4.9 (5)
S450	38	19.1 (5)	20.0 (5)
S500	40	20.2 (5)	21.1 (5)
S550	42	21.6 (5)	22.6 (5)
S600	50	25.2 (5)	26.4 (5)

a well-defined and sharp maximum characteristic of non-interacting magnetic NPs (Fig. 11) and an irreversibility temperature almost coinciding with the blocking temperature ($T_{irr} \approx T_B$). The origin of this non-interacting regime could be ascribed to the "screening" effect provoked by the non-magnetic Ni-HCP and Ni_3C layers covering the Ni-FCC core spins. In contrast, sample S600 displays a huge difference between T_{irr} and T_B (almost four times larger), suggesting that the decrease of non-magnetic Ni-based phases favours the magnetic coupling between the Ni-FCC NP spins. The samples synthesized at intermediated temperatures show a progressive change in the magnetic coupling (Fig. 11).

Based on the Stoner–Wohlfarth model[50–52] we have refined the temperature dependence of the magnetization under ZFC/FC regimes (solid lines in Fig. 11) using the NP size distribution obtained above (see Table 1 and Fig. 3). The calculated curves are in excellent agreement with the experimental data, thus providing information about the magnitude and evolution of the effective magnetic anisotropy energy. While bulk Ni-FCC has a value of around 10^6 erg cm^{-3}, and that of the S400 sample is well below this ($\approx 10^4$ erg cm^{-3}) and increases progressively to *ca.* 10^5 erg cm^{-3} for the S600 sample. This difference can be explained by a change in the different (bulk, surface, and shape) contributions to the effective magnetic anisotropy, thus confirming the abovementioned change of physical regime, from non-interacting to interacting magnetic Ni-FCC NPs. This feature is clear evidence of the role played by the carbonaceous environment and the modification of the microstructure of the NPs produced at the carbonization temperature rises.

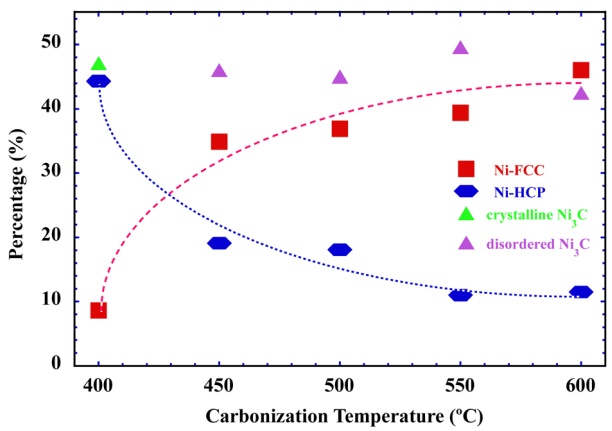

Fig. 10 Evolution of the weight-percentages of the Ni-based phases with the carbonization temperature (see text).

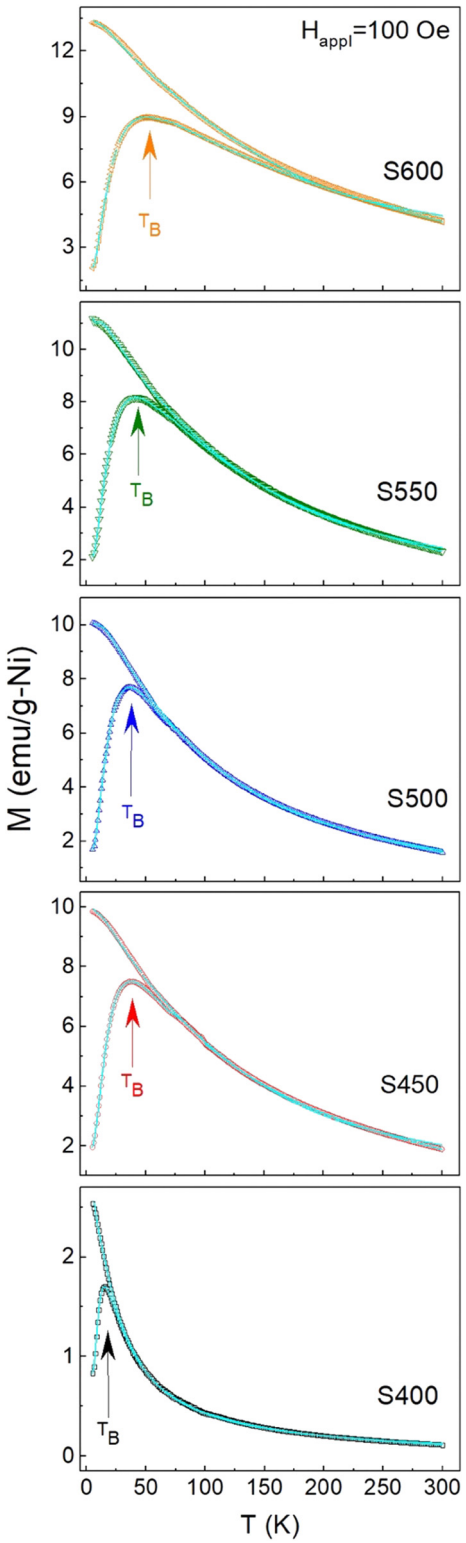

Fig. 11 $M(T)$ curves measured in the ZFC and FC regime under an applied magnetic field, H_{appl} = 100 Oe. The dots correspond to the experimental data, while the solid line is associated with the Stoner–Wohlfarth-based fit. Arrows point out the average blocking temperatures (T_B). (see text for details).

Summary and conclusions

The investigated Ni nanoparticles embedded in a carbonaceous matrix represent a good example of the difficulty in determining the intricate relationship between the structure and magnetism in multicomponent systems. Therefore, it appears highly necessary to develop cross checks between different experimental techniques. An important characteristic of these complementary probes is not to introduce too much additional parameters besides those which are the relevant ones.

The main result of the current joint analysis using X-ray diffraction, HRTEM analysis and magnetic measurements is that the carbonization temperature not only plays a leading role in the amount of Ni, but also in the crystalline nature of the three coexisting phases (Ni_3C, Ni-HCP and Ni-FCC), the formation of an exotic ''artichoke-like'' morphology, the size distribution of the nanoparticles, and their magnetic behaviour. In fact, for sample S400 the Ni_3C phase is almost certainly present in two different crystal structures, rhombohedral and hexagonal, with major crystallinity. However, for carbonization temperatures above 400 °C this Ni_3C phase loses long-range crystalline order, becoming a sort of disordered solid solution in which Ni atoms are retained and do not contribute to the magnetization of the samples, that comes exclusively from the ferromagnetic Ni-FCC crystalline phase.

Additionally, it is worth noting the formation of several concentric turbostratic carbon layers covering the nanoparticles, which serve as robust protection layers against nickel oxidation, contrary to what is seen in Ni-NP systems synthesized through conventional chemical routes that exhibit a typical Ni@NiO core–shell morphology, and the concomitant emergence of a magnetic exchange-bias effect. The last and most conceptually important point concerns the role of nickel–carbon interconnection in the physical–chemical properties of these nanoparticles. Our findings lead us to conclude that the present Ni@C hybrid introduces, not just some features that have to do with the protection against oxidation, but also features that promote the blockage of an important number of Ni atoms, which therefore become non-magnetic, in contrast to what is usually seen for common metallic nickel. As a result, the present investigation based on a detailed and rigorous analysis of the magnetic data helps in understanding the role that different phases play in these Ni@C samples and could pave the way for the search for other Ni-based nanostructured systems in carbonaceous matrices that might be potentially used in a variety of technological applications.

Author contributions

M. F. performed magnetic measurements and collected the data; she also carried out most of the data analysis and prepared the original draft of the manuscript. P. G., J. A. B. & J. I. P. & F. S.-G. were co-responsible for the conceptualization and methodology of the work. P. G., J. A. B., J. I. P. & J. P. A. were responsible for funding acquisition and supervision of the work. F. J. M.-J. synthesized the samples. D. M.-B. performed XRD experiments and contributed to data analysis. A. A. collected TEM/HRTEM images and performed detailed analysis of the images. M. P. F.-G., J. H. B. and P. A.-A. were responsible for the analysis of the magnetic data. All authors participated in the writing, review and editing of the final version of the manuscript.

Conflicts of interest

There are no conflicts to declare.

Acknowledgements

This work was supported by the Spanish MICINN, Agencia Estatal de Investigación (AEI) and the European Regional Development Fund (ERDF) through projects RTI2018-094683-B-C52 (Univ. Oviedo) & RTI2018-100832-B-I00 (INCAR-CSIC), as well as by the Plan de Ciencia, Tecnología e Innovación (PCTI) 2018-2022 del Principado de Asturias and the ERDF through projects AYUD/2021/51822 (Univ. Oviedo) and IDI/2021/000037 (INCAR-CSIC). A. Adawy acknowledges the financial support received from research projects MCI-21-PID2020-113558RB-C41 (MICINN) and GRUPIN-IDI/2018/170 (Principado de Asturias) to pursue her work at the Univ. Oviedo.

Notes and references

1 N.-D. Jaji, H. L. Lee, M. H. Hussin, H. M. Akil, M. R. Zakaria and M. B. H. Othman, *Nanotechnol. Rev.*, 2020, **9**, 1456.
2 Z. Zhu, Z. Li, X. Wei, J. Wang, S. Xiao, R. Li, R. Wu and J. S. Chen, *Carbon*, 2021, **185**, 9.
3 A. Dahal and M. Batzill, *Nanoscale*, 2014, **6**, 2548.
4 Z. Xiang, X. Zhang, Y. Shi, L. Cai, J. Cheng, H. Jiang, X. Zhu, Y. Dong and W. Lu, *Carbon*, 2021, **185**, 477.
5 P. Gorria, M. Sevilla, J. A. Blanco and A. B. Fuertes, *Carbon*, 2006, **44**, 1954.
6 M. R. Ahghari, V. Soltaninejad and A. Maleki, *Sci. Rep.*, 2020, **10**, 12627.
7 H. Yan, Y. Dong, L. Cai, F. Pan and W. Lu, *Carbon*, 2022, **200**, 317.
8 B. Roldan-Cuenya, *Thin Solid Films*, 2010, **518**, 3127.
9 K. H. Oh, H.-K. Lee, S. W. Kang, J.-I. Yang, G. Nam, T. Lim, S. H. Lee, C. S. Hong and J. C. Park, *J. Ind. Eng. Chem.*, 2022, **106**, 449.
10 B. Feng, R. Guo, Q. Cai, Y. Song, N. Li, Y. Fu, D.-L. Chen, J. Zhang, W. Zhu and F. Zhang, *Nano Res.*, 2022, **15**, 6001.
11 Y. Tian, Y. Liu, F. Pan, F. Wan and X. Zhang, *Colloids Surf., A*, 2015, **464**, 96.
12 Y. Wang, X. Di, J. Chen, L. She, H. Pan, B. Zhao and R. Che, *Carbon*, 2022, **191**, 625.
13 N. Wang, Y. Wang, Z. Lu, R. Cheng, L. Yang and Y. Li, *Carbon*, 2023, **202**, 254.
14 W. Wang, Y. Wang, Z. Lu, R. Cheng and H. Zheng, *Carbon*, 2023, **203**, 397.

15 K. Shen, X. Chen, J. Chen and Y. Li, *ACS Catal.*, 2016, **6**, 5887.
16 M. Y. Zong, C. Z. Fan, X. F. Yang and D. H. Wang, *Mol. Catal.*, 2021, **509**, 111609.
17 M. H. Shahini, H. E. Mohammadloo, M. Ramezanzadeh and B. Ramezanzadeh, *Mater. Chem. Phys.*, 2022, **276**, 125420.
18 P. Gorria, M. P. Fernandez-Garcia, M. Sevilla, J. A. Blanco and A. B. Fuertes, *Phys. Status Solidi RRL*, 2009, **3**, 4.
19 F. J. Martín-Jimeno, F. Suárez-García, J. I. Paredes, A. Martínez-Alonso and J. M. D. Tascón, *J. Alloys Compd.*, 2021, **853**, 157348.
20 R. T. Chiang, R. K. Chiang and F. S. Shieu, *RSC Adv.*, 2014, **4**, 19488.
21 J. G. Wright and J. Goddard, *Philos. Mag.*, 1965, **11**, 485.
22 J. Gong, L. L. Wang, Y. Liu, J. H. Yang and Z. G. Zong, *J. Alloys Compd.*, 2008, **457**, 6.
23 A. Kotoulas, M. Gjoka, K. Simeonidis, I. Tsiaussis, M. Angelakeris, O. Kalogirou and C. Dendrinou-Samara, *J. Nanopart. Res.*, 2011, **13**, 1897.
24 Y. T. Jeon, J. Y. Moon, G. H. Lee, J. Park and Y. M. Chang, *J. Phys. Chem. B*, 2006, **110**, 1187.
25 Y. Goto, K. Taniguchi, T. Omata, S. Otsuka-Yao-Matsuo, N. Ohashi, S. Ueda, H. Yoshikawa, Y. Yamashita, H. Oohashi and K. Kobayashi, *Chem. Mater.*, 2008, **20**, 4156.
26 L. Yue, R. Sabiryanov, E. M. Kirkpatrick and D. L. Leslie-Pelecky, *Phys. Rev. B: Condens. Matter Mater. Phys.*, 2000, **62**, 8969.
27 Z. L. Schaefer, K. M. Weeber, R. Misra, P. Schiffer and R. E. Schaak, *Chem. Mater.*, 2011, **23**, 2475.
28 L. He, *J. Magn. Magn. Mater.*, 2010, **322**, 1991.
29 Z. Xiang, C. Huang, Y. Song, B. Deng, X. Zhang, X. Zhu, D. Batalu, O. Tutunaru and W. Lu, *Carbon*, 2020, **167**, 364.
30 S. Gao, G. Zhang, Y. Wang, X. Han, Y. Huang and P. Liu, *J. Mater. Sci. Technol.*, 2021, **88**, 56.
31 D. A. Papaconstantopoulus, J. L. Fry and N. E. Brener, *Phys. Rev. B: Condens. Matter Mater. Phys.*, 1989, **39**, 2526.
32 X. He, L. T. Kong and B. X. Liu, *J. Appl. Phys.*, 2005, **97**, 106107.
33 C. N. Chinnasamy, B. Jeyadevan, K. Shinova, K. Tohji, A. Narayanasamy, K. Sato and S. Hisano, *J. Appl. Phys.*, 2005, **97**, 10J309.
34 M. Han, Q. Liu, J. H. He, Y. Song, Z. Xu and J. M. Zhu, *Adv. Mater.*, 2007, **19**, 1096.
35 Y. Mi, D. Yuan, Y. Liu, J. Zhang and Y. Xiao, *Mater. Chem. Phys.*, 2005, **89**, 359.
36 S. Fujieda, T. Kuboniwa, K. Shinoda, S. Suzuki and J. Echigoya, *AIP Adv.*, 2016, **6**, 056116.
37 Y. Zhang, Y. Zhu, Y. Cao, D. Li, Z. Zhang, K. Wang, F. Ding, X. Wang, D. Meng, L. Fan and J. Wu, *RSC Adv.*, 2016, **6**, 81989.
38 S. Fujieda, K. Shinoda, S. Suzuki and B. Jeyadevan, *Mater. Trans.*, 2012, **53**, 1716.
39 J. Rodriguez-Carvajal, *Physica B*, 1993, **192**, 55.
40 D. Martinez-Blanco, P. Gorria, J. A. Blanco, M. J. Perez and J. Campo, *J. Phys.: Condens. Matter*, 2008, **20**, 335213.
41 C. A. Schneider, W. S. Rasband and K. W. Eliceiri, *Nat. Methods*, 2012, **9**, 671.
42 N. Rinaldi-Montes, P. Gorria, D. Martinez-Blanco, A. B. Fuertes, L. Fernandez Barquin, J. Rodriguez Fernandez, I. de Pedro, M. L. Fdez-Gubieda, J. Alonso, L. Olivi, G. Aquilanti and J. A. Blanco, *Nanoscale*, 2014, **6**, 457.
43 N. Rinaldi-Montes, P. Gorria, A. B. Fuertes, D. Martínez-Blanco, Z. Amghouz, I. Puente-Orench, L. Olivi, J. Herrero-Martin, M. P. Fernandez-Garcia, J. Alonso, M.-H. Phan, H. Srikanth, X. Marti and J. A. Blanco, *J. Mater. Chem. C*, 2022, **10**, 1798.
44 C. Ballesteros, A. Zern, A. Garcıa-Escorial, A. Hernando and J. M. Rojo, *Phys. Rev. B: Condens. Matter Mater. Phys.*, 1998, **58**, 89.
45 J. M. Rojo, A. Hernando, M. El Ghannami, A. Garcıa-Escorial, M. A. González, R. García-Martínez and L. Ricciarelli, *Phys. Rev. Lett.*, 1996, **76**, 4833.
46 M. P. Fernandez-Garcia, P. Gorria, M. Sevilla, M. P. Proença, R. Boada, J. Chaboy, A. B. Fuertes and J. A. Blanco, *J. Phys. Chem. C*, 2011, **115**, 5294.
47 A. Ghogia, L. M. Romero Millán, C. E. White and A. Nzihou, *ChemSusChem*, 2022, e202201864.
48 N. Rinaldi-Montes, P. Gorria, D. Martinez-Blanco, Z. Amghouz, A. B. Fuertes, L. Fernandez Barquin, I. de Pedro, L. Olivi and J. A. Blanco, *J. Mater. Chem. C*, 2015, **3**, 5674.
49 B. D. Cullity, *Introduction to Magnetic Materials*, Addison-Wesley, Reading MA, 2009.
50 M. Respaud, J. M. Broto, H. Rakoto, A. R. Fert, L. Thomas, B. Barbara, M. Verelst, E. Snoeck, P. Lecante, A. Mosset, J. Osuna, T. Ould Ely, C. Amiens and B. Chaudret, *Phys. Rev. B: Condens. Matter Mater. Phys.*, 1998, **57**, 2925.
51 C. de Julián Fernández, *Phys. Rev. B: Condens. Matter Mater. Phys.*, 2005, **72**, 054438.
52 K. L. Livesey, S. Ruta, N. R. Anderson, D. Baldomir, R. W. Chantrell and D. Serantes, *Sci. Rep.*, 2018, **8**, 11166.

